

# Chiral properties of the zero-field spiral state and field-induced magnetic phases of the itinerant kagome metal $\text{YMn}_6\text{Sn}_6$

Rebecca L. Dally <sup>\*</sup> and Jeffrey W. Lynn 

*Center for Neutron Research, National Institute of Standards and Technology, Gaithersburg, Maryland 20899, USA*

Nirmal J. Ghimire , Dina Michel , Peter Siegfried , and Igor I. Mazin

*Department of Physics and Astronomy, George Mason University, Fairfax, Virginia 22030, USA  
and Quantum Science and Engineering Center, George Mason University, Fairfax, Virginia 22030, USA*



(Received 23 December 2020; revised 22 February 2021; accepted 23 February 2021; published 8 March 2021)

Applying a magnetic field in the hexagonal plane of  $\text{YMn}_6\text{Sn}_6$  leads to a complex magnetic phase diagram of commensurate and incommensurate phases, one of which coexists with the topological Hall effect (THE) generated by a unique fluctuation-driven mechanism. Using unpolarized neutron diffraction, we report on the solved magnetic structure for two previously identified, but unknown, commensurate phases. These include a low-temperature, high-field fanlike phase and a room-temperature, low-field canted antiferromagnetic phase. An intermediate incommensurate phase between the fanlike and forced ferromagnetic phases is also identified as the last known phase of the in-plane field-temperature diagram. Additional characterization using synchrotron powder diffraction reveals extremely high-quality, single-phase crystals, which suggests that the presence of two incommensurate magnetic structures throughout much of the phase diagram is an intrinsic property of the system. Interestingly, polarized neutron diffraction shows that the centrosymmetric system hosts preferential chirality in the zero-field double-flat-spiral phase, which, along with the THE, is a topologically nontrivial characteristic.

DOI: [10.1103/PhysRevB.103.094413](https://doi.org/10.1103/PhysRevB.103.094413)

## I. INTRODUCTION

Verifying the correct ground state for magnetic systems with competing interactions has been a fundamental problem since the triangular Ising antiferromagnet was first studied 70 years ago. This is an example of antiferromagnetic (AFM) interactions on a particular lattice geometry that leads to magnetic frustration, e.g., geometrical frustration. Moving beyond frustration due solely to geometrical restrictions combined with AFM interactions, one can look to competing nearest-neighbor and next-nearest-neighbor—and farther—interactions, which can lead to either no order as is the case in spin liquids, short-range order, or even a multiphase space, where either side of a phase boundary line represents two different orderings with subtle energetic differences. Often, the structure which emerges from the frustration is a long-wavelength incommensurate spin texture, where the details of the underlying crystal lattice symmetry determine additional expressed features [1], such as chiral handedness [2,3], the magnetoelectric effect [4,5], toroidal order [6], and nonreciprocal magnons [7,8]. These are examples of phenomena which occur when magnetism is in the presence of broken spatial inversion symmetry (i.e., noncentrosymmetric lattices).

More recently, magnetic frustration in centrosymmetric systems has been theorized, and experimentally verified, as a route to stabilize topologically protected skyrmion lattices [9–11], a phase that traditionally materialized from chiral

crystal structures. Similarly, topologically nontrivial multi- $\mathbf{q}$  structures, other than the canonical triple  $\mathbf{q}$  of the skyrmion lattice, and in the absence of the Dzyaloshinskii-Moriya antisymmetric exchange interaction, have also been reported [12]. It is then natural to ask whether other topological properties that require broken inversion symmetry can be found in centrosymmetric, frustrated magnet systems. For example, the topological Hall effect (THE) was recently observed in  $\text{YMn}_6\text{Sn}_6$  [13,14], a centrosymmetric (space group  $P6/mmm$ ) itinerant helimagnet, with the maximum effect occurring around 245 K and an applied field of about 4 T in the  $ab$  plane. Although no skyrmion lattice was found in this region of phase space, a noncoplanar spin texture was: a transverse conical spiral (TCS) [13,14]. This spin texture would not on its own lead to the THE, but it was argued that dynamic chiral fluctuations are responsible, thus making  $\text{YMn}_6\text{Sn}_6$  a prototype material for a fluctuation based THE mechanism. Thermal fluctuations, coupled with the strongly two-dimensional nature of the magnetic exchange, are thought to be key ingredients for realizing the THE despite the null scalar spin chirality in the absence of an external field. It is then the addition of unbalanced magnon fluctuations in the transverse conical phase which creates a nonzero chiral susceptibility.

Shown in Fig. 1(a),  $\text{YMn}_6\text{Sn}_6$  is composed of Mn atoms on a kagome lattice in the  $ab$  plane, which are then stacked along the  $c$  axis with the layers separated either by three Sn layers ( $\text{Sn}_3$ ) or a mixed Y and Sn layer ( $\text{Sn}_2\text{Y}$ ). Mn atoms in plane are at equivalent positions and are strongly coupled ferromagnetically via nearest-neighbor exchange ( $J_p < 0$ ) and

<sup>\*</sup>Corresponding author: [rebecca.dally@nist.gov](mailto:rebecca.dally@nist.gov)

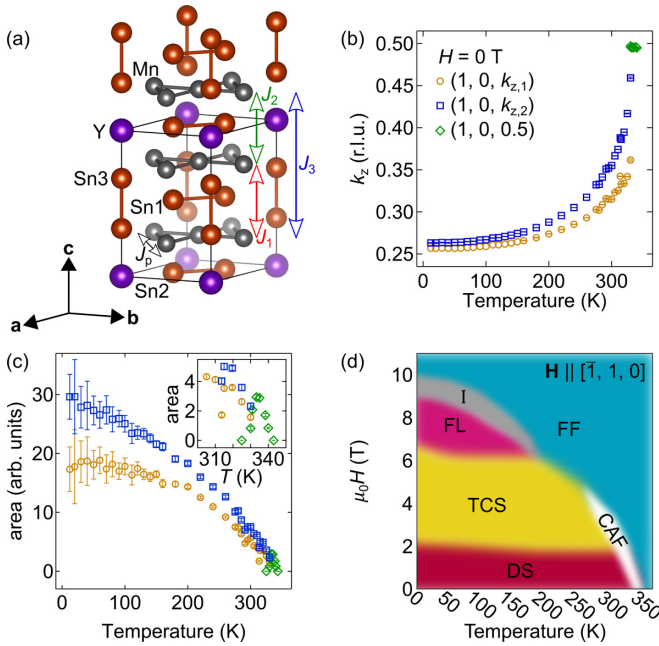


FIG. 1. (a) Crystal structure of  $\text{YMn}_6\text{Sn}_6$ , belonging to space group  $P6/mmm$  (191). The Mn-Mn magnetic exchange pathways as discussed in the main text are indicated by the arrows and labels,  $J_p$  and  $J_1$ - $J_3$ . Single-crystal neutron-diffraction data showing the temperature dependence of the magnetic (b) wave vectors and (c) Bragg peak intensities in zero-field conditions. The inset of (c) shows the progression of the magnetic structures just below  $T_N \approx 340$  K. One commensurate structure emerges at  $T_N$ , but it is short lived and quickly gives way with decreasing temperature to two incommensurate structures. The legend for (c) is the same as in (b). (d) Magnetic structure phase diagram for the applied field,  $\mathbf{H}$ , in plane. The neutron-diffraction experiments in this paper were carried out with  $\mathbf{H} \parallel [\bar{1}, 1, 0]$ . The phases DS, TCS, FL, CAF, I, and FF correspond to distorted spiral, transverse conical spiral, fanlike, canted antiferromagnet, phase I, and forced ferromagnetic, respectively.

have the spins in the  $ab$  plane due to easy-plane anisotropy ( $K < 0$ ). This stacking pattern has an important magnetic implication, mainly, that within a unit cell there are two unequal interlayer exchange pathways with opposite signs. The interaction across the  $\text{Sn}_3$  layer is ferromagnetic (FM) ( $J_1 < 0$ ) and across the  $\text{Sn}_2\text{Y}$  layer it is antiferromagnetic ( $J_2 > 0$ ). These exchange parameters alone would be compatible with a commensurate antiferromagnetic structure, where the magnetic unit cell is doubled along the  $c$  axis. Indeed, this is the initial magnetic structure just below the Néel temperature ( $T_N \approx 340$  K). However, the interlayer coupling between like-Mn layers is ferromagnetic ( $J_3 < 0$ ), and below 333 K the exchange competition drives the system into a double-flat-spiral magnetic structure. In this structure, two rotation angles are needed to describe the directions of the spins (see, for example, Ref. [15]). One angle defines the relative difference between the two layers of spins within the unit cell, and the second angle defines the relative difference between the layers of spins in adjacent unit cells, and these angles are highly temperature dependent in  $\text{YMn}_6\text{Sn}_6$ . Curiously, the transition to this incommensurate structure sees two double-flat-spirals

emerge:  $\mathbf{k}_1 = (0, 0, k_{z,1})$  and  $\mathbf{k}_2 = (0, 0, k_{z,2})$ , where  $k_{z,1}$  and  $k_{z,2}$  are almost the same, and both are long range [14,16–18]. Single-crystal neutron diffraction data in Figs. 1(b) and 1(c) show the transition from the commensurate to incommensurate structure by tracking the wave vectors and magnetic Bragg peak intensities at the  $(1, 0, 0) + \mathbf{k}$  positions. The wave vectors for the incommensurate structures are strongly temperature dependent, getting closer with decreasing temperature, but never merge (at least to 12 K), and they have similar in-field behavior.

Upon application of an external magnetic field in the  $ab$  plane, the magnetic phase diagram becomes much more complex [see Fig. 1(d)]. A previous study identified five new magnetic phases via ac susceptibility measurements [14], and through theoretical and neutron-diffraction studies was able to predict/confirm the structure of some of those phases. Here we present the solved magnetic structures for two of the in-field phases previously identified but unsolved, namely, phase “II”—from here on out denoted canted antiferromagnet (CAF)—and fanlike (FL), using single-crystal unpolarized neutron-diffraction measurements. Additionally, we were able to identify the change in magnetic structure that leads to the region of the ac-susceptibility phase diagram called phase “I.”

We also present a result obtained via a polarized neutron-diffraction study. Unexpectedly, unequal chiral domain populations of the zero-field spiral state were found despite the underlying centrosymmetric crystal symmetry. This could be a significant finding as it implies that the spiral state can energetically favor one domain over the other, possibly in a controlled manner. This is another example, along with the THE, of  $\text{YMn}_6\text{Sn}_6$  displaying unusual behavior for a structure with inversion symmetry.

## II. EXPERIMENTAL DETAILS

Single crystals of  $\text{YMn}_6\text{Sn}_6$  were grown by the self-flux method described in Ref. [14], and all neutron experiments used the same 70 mg crystal. The flat side of this platelike crystal was mounted flush with a thin aluminum plate and attached using thin aluminum wire. For all data, error bars represent plus and minus one standard deviation of uncertainty.

Data for Figs. 1(b) and 1(c) were taken using a single crystal oriented in the  $(H, 0, L)$  scattering plane on the BT-7 triple-axis spectrometer at the NIST Center for Neutron Research [19]. Elastic diffraction measurements were performed using  $E_i = E_f = 14.7$  meV with open- $25'-25'-120'$  collimation before the monochromator, sample, analyzer, and detector, respectively. All other neutron data, with the exception of Fig. 5, were taken using a single-crystal oriented in the  $(H, H, L)$  scattering plane with  $25'-25'-25'-25'$  collimation.

A 10-T superconducting vertical field magnet was used to take in-field measurements where the field was parallel to the crystallographic  $[\bar{1}, 1, 0]$  direction. The high sample quality resulted in a sharp mosaic, and data for the magnetic structure determination were taken as  $\theta - 2\theta$  scans through the Bragg peaks. To extract the intensity proportional to the structure factor squared, integrated Bragg peak intensities were corrected by the Lorentz factor ( $I_{hkl}^{\text{obs}} \propto \frac{|F_{hkl}|^2}{\sin 2\theta_{hkl}}$ ). These values were used to refine structures with the Rietveld method and

the program FULLPROF [20], and the free-ion form factor for  $\text{Mn}^{2+}$  was used in magnetic refinements. Measurements of the nuclear Bragg peaks at 0 T revealed that extinction effects, and possibly multiple Bragg scattering, diminished the intensity of the strongest peaks; thus, any magnetic intensity appearing at these positions upon application of the field was excluded from refinement for the in-field structure determinations.

The beam for the polarized neutron diffraction measurements was created using a  $^3\text{He}$  polarizer before the sample, and polarization analysis was made possible using an additional  $^3\text{He}$  polarizer after the sample [21]. A guide field of 1 mT was employed to define the polarization axis and was oriented in plane and along the scattered wave vector, or perpendicular to the scattering plane. Initial flipping ratios were typically  $\approx 34$ . The four neutron scattering cross sections available for measurement were  $I^{++}$ ,  $I^{+-}$ ,  $I^{-+}$ , and  $I^{--}$ . Data were taken with the scattering vector,  $\mathbf{Q}$ , both parallel and perpendicular to the neutron polarization,  $\mathbf{P}$ , and the temperature was held constant at 290 K. All data were corrected for polarization efficiency before analysis. Both nuclear and magnetic Bragg peaks were resolution limited, and Voigt functions were used to fit the data.

High-resolution synchrotron powder diffraction data were collected using beamline 11-BM at the Advanced Photon Source at Argonne National Laboratory using a wavelength of 0.4579 Å. Due to the high absorption of Sn at this wavelength, samples were prepared by coating the outside of a 0.8 mm diameter Kapton capillary with a mixture of sample powder (a ground single crystal of  $\text{YMn}_6\text{Sn}_6$ ) and Dow Corning 4 Electrical Insulating Compound silicone grease. Refinement of the data was performed using the program FULLPROF [20]. All data sets (temperatures) were first refined using a Le Bail fit in order to obtain the lattice and peak profile parameters and the background. It was found that the peaks could be fully described by a Lorentzian profile and that some peak width anisotropy was present, where  $(0, 0, L)$ -type peaks tended to be slightly narrower than others. A spherical harmonics size-broadening model was able to capture the peak profile shape correctly for all peaks. The profile and background parameters were then used, and held constant, for the Rietveld refinement. Lattice parameters, anisotropic atomic displacement parameters, and Sn occupancies were allowed to refine. An impurity phase from elemental Sn, which was used during flux growth, was also included in the refinement, and found to be  $\approx 7\%$ .

### III. RESULTS

#### A. In-field magnetic structures

##### 1. Room-temperature, low-field canted antiferromagnetic phase

Previous ac susceptibility and neutron diffraction measurements identified a small region of finite field-temperature phase space with a commensurate magnetic structure and wave vector of  $(0, 0, 0.5)$  [14]. The phase was labeled “II” and was stabilized at fields ranging between  $\approx 2$  T and 4 T and spanned temperatures between  $\approx 250$  K and 320 K. We have studied the field-dependent onset of the phase at 295 K and have solved the magnetic structure at 3 T.

An important note is that all incommensurate phases are present with two wave vectors,  $\mathbf{k}_1 = (0, 0, k_{z,1})$  and  $\mathbf{k}_2 =$

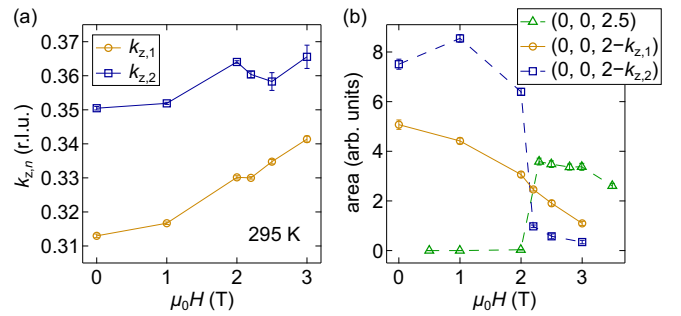


FIG. 2. Room-temperature data showing the evolution of the magnetic structures with increasing applied field. (a) The change in periodicity for the two incommensurate structures with wave vectors  $(0, 0, k_{z,n})$ . (b) The change in intensity for magnetic Bragg peaks about the  $(0, 0, 2)$  reciprocal-lattice point. As the Bragg peak at  $(0, 0, 2 - k_{z,2})$  rapidly decreases in intensity above 2 T, the commensurate Bragg peak at  $(0, 0, 2.5)$  just as rapidly increases in intensity. The dashed lines for both data sets are to emphasize the relationship between the two, which suggests the incommensurate  $k_{z,2}$  structure is transitioning into the commensurate structure above 2 T.

$(0, 0, k_{z,2})$ , where  $|k_{z,1}| < |k_{z,2}|$  for all temperatures with and without applied magnetic field. Due to the proximity to each other, the high-resolution measurements presented here are needed to resolve the Bragg peaks associated with each wave vector. As such, the periodicity of the incommensurate wave vectors was tracked as a function of field, shown in Fig. 2(a). For both incommensurate structures, the period of the spiral is generally shortened with increasing field, with the exception of a short-lived increase between 2 T and 2.2 T. It is between these fields that the commensurate structure abruptly emerges, as shown by the field-dependent intensity data of the  $(0, 0, 2.5)$  magnetic Bragg peak in Fig. 2(b). As the commensurate structure sets in, the incommensurate structure associated with  $k_{z,2}$  loses most of its intensity, indicating a phase transition of this incommensurate structure to the commensurate one. Meanwhile, the incommensurate structure associated with  $k_{z,1}$  monotonically and smoothly decreases in intensity with applied field.

The Rietveld refined fit and structure are depicted in Fig. 3. The best-fit magnetic structure was found to have the same AFM coupling as the high-temperature, zero-field structure which initially sets in with the onset of long-range order at  $T_N$ . That is, magnetic ions through the  $\text{Sn}_3$  layer are FM coupled, and ions through the  $\text{Sn}_2\text{Y}$  layer are AFM coupled. All ions within a layer are FM coupled, as is the case for all the reported  $\text{YMn}_6\text{Sn}_6$  magnetic phases. Due to the applied field, the moments are all canted towards the field direction, adding a net ferromagnetic component and second commensurate wave vector,  $\mathbf{k} = 0$ . The angle the moments make with the applied field direction is denoted  $\gamma$ . The moments through the  $\text{Sn}_2\text{Y}$  layer (the AFM coupled layers) were constrained during refinement such that the angles away from  $\mathbf{H}$  both had a magnitude of  $\gamma$  and all moments were constrained to have the same magnitude. The refined angle,  $\gamma = 52(2)^\circ$ , and the refined moment,  $\mu = 1.13(4)\mu_B$ , resulted in a fit with an  $R$  factor of 9.21.

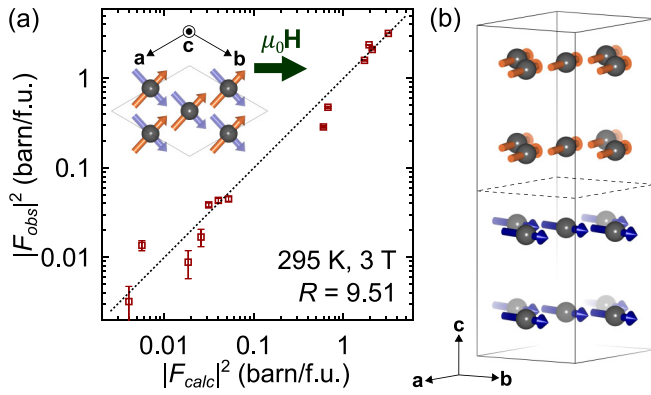


FIG. 3. Results of the best-fit magnetic model for the room-temperature, low-field canted antiferromagnetic phase with wave vectors,  $(0, 0, 0)$  and  $(0, 0, 0.5)$ . Data were taken at 295 K and 2 T in the  $(H, H, L)$  scattering plane, and the figures represent the magnetic structure at this particular field and temperature. (a) The observed vs calculated magnetic structure factor squared in barn/formula unit (f.u.). The calculated result was obtained via Rietveld refinement for the magnetic intensity only. The inset shows the magnetic structure in the  $ab$  plane. Only Mn ions are shown (gray spheres), and the orange and blue arrows represent the two different directions of the moments. (b) The magnetic unit cell, where the dashed line defines the size of the nuclear unit cell.

## 2. Low-temperature, high-field fanlike phase

The low-temperature, high-field commensurate magnetic phase was denoted “fan-like” in Ref. [14]. It can be described with wave vectors  $(0, 0, 0)$  and  $(0, 0, 0.25)$ , and an additional modulation within the  $4c$  periodicity resulted in  $(0, 0, 0.5)$ -type magnetic Bragg peaks. The region of phase space spanned by this phase is much larger than the CAF phase previously discussed. Data presented here were taken at 1.5 K and 7.8 T, where there was no trace of any incommensurate structure.

The theoretical model in Ref. [14] found a stable magnetic structure matching the periodicity of the observed magnetic Bragg peaks. The moment directions for the eight layers of Mn atoms within the magnetic unit cell could be described by angles  $\gamma, \gamma, -\delta, \delta, -\gamma, -\gamma, \delta$ , and  $-\delta$ , which are measured with respect to the field direction. This structure is viewed in Fig. 4 where orange and blue arrows represent moments, the directions of which can be defined by either the angle  $\gamma$  or  $\delta$ , respectively. The refined fit for this model (model 1) is shown in Fig. 4(a) with  $\gamma = 68(2)^\circ$ ,  $\delta = 0(1)^\circ$ ,  $\mu = 1.95(5)\mu_B$ , and an  $R$  factor of 12.4. All moments were constrained to have the same magnitude.

Another model, model 2, resulted in a similar goodness of fit ( $R$  factor = 12.1, see the Appendix). The relationship between angles in this model can be described as  $\gamma, \gamma, -\delta, -\delta, -\gamma, -\gamma, \delta$ , and  $\delta$ , with refined values  $\gamma = 69(3)^\circ$ ,  $\delta = 12(6)^\circ$ , and  $\mu = 1.91(6)\mu_B$ . The magnetic structure factors for both models are almost identical. If  $\gamma, \delta$ , and  $\mu$  were the same for both models, the structure factors for  $(0, 0, 0)$ -type and  $(0, 0, 0.5)$ -type peaks would also be the same. The structure factors would only differ for the  $(0, 0, 0.25)$ -type peaks, but as  $\delta \rightarrow 0$  in model 1 the structure factors for these peaks

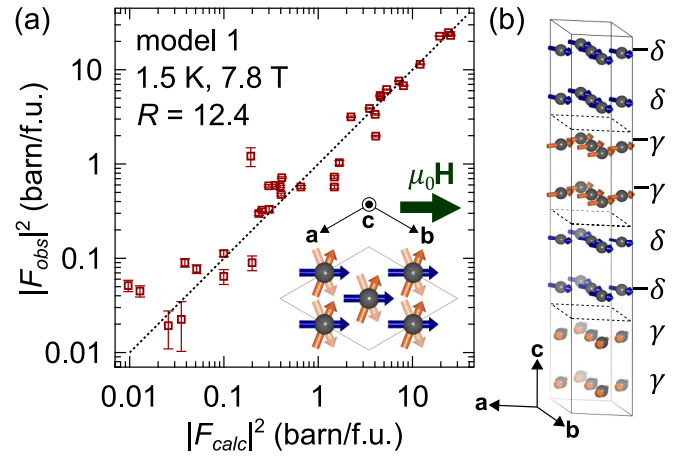


FIG. 4. Results for model 1 of the low-temperature, high-field fanlike phase with wave vectors,  $(0, 0, 0)$ ,  $(0, 0, 0.25)$ , and  $(0, 0, 0.5)$ . Data were taken at 1.5 K and 7.8 T in the  $(H, H, L)$  scattering plane. (a) The observed vs calculated magnetic structure factor squared in barn/formula unit (f.u.). The calculated result was obtained via Rietveld refinement for the magnetic intensity only. The inset shows the refined magnetic structure in the  $ab$  plane for 1.5 K and 7.8 T, where  $\gamma = 68(2)^\circ$  and  $\delta = 0(1)^\circ$ . Only Mn ions are shown (gray spheres), and the orange and blue arrows represent the two different angle magnitudes,  $\gamma$  and  $\delta$ , respectively, which define the moment directions away from the applied field direction. (b) The magnetic unit cell, where the dashed lines define the size of the nuclear unit cell.

converge to that of model 2. Details of the structure factor calculations can be found in the Appendix.

## 3. Phase I

We now comment on the “I” region of the phase diagram in Fig. 1(b). Data in Fig. 5 were taken at 10 K and show an intermediate magnetic structure between the FL phase, at 9.0 T and 9.5 T, and the forced ferromagnetic (FF) phase, at 10.5 T. At 10.0 T, the 0.5-type Bragg peak at  $(0, 0, 2.5)$  is

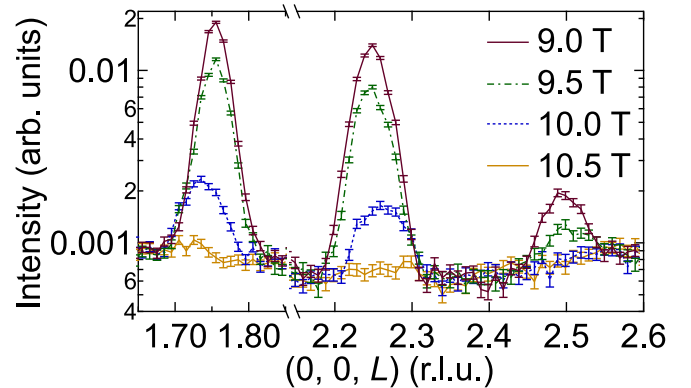


FIG. 5. High-field data with  $\mathbf{H} \parallel [\bar{1}, 1, 0]$ , taken at 10 K with a position sensitive detector and moderately coarse resolution. Between the FL phase (9.0 T and 9.5 T) and FF phase (10.5 T), an intermediate phase appears, where the 0.5-like peaks disappear, and the magnetic structure is incommensurate. Lines connect between marker points for clarity.

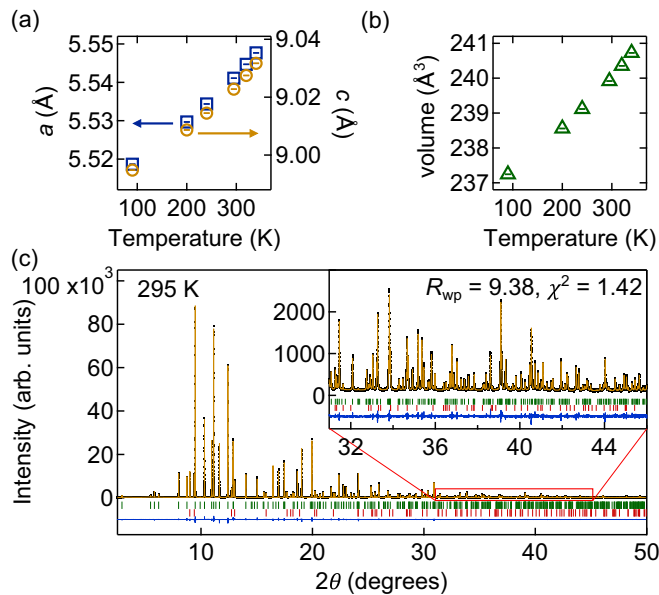


FIG. 6. Results from the analyzed synchrotron powder diffraction data. (a) The lattice parameters and (b) unit-cell volume vs temperature. (c) Rietveld refinement for 295-K data. The data are displayed as black dots and the Rietveld calculated fit is the solid yellow line running through the data. The top row of tick marks (green) denotes  $\text{YMn}_6\text{Sn}_6$  Bragg peak positions, and the bottom row of tick marks (red) denotes the elemental Sn impurity Bragg peak positions. The difference curve (observed-calculated) is shown as the solid blue line on the bottom of the plot. The inset highlights the fit in the high- $Q$  region.

completely gone, and the peaks at 0.25-type positions have shifted away from the zone centers to become, once again, incommensurate. The positions of the incommensurate peaks shown are at  $L = 1.7335(8)$  and  $2.266(1)$ , which correspond to an average wave vector of  $\mathbf{k} \approx (0, 0, 0.26)$ , the same as the average of the two zero-field wave vectors at this temperature [14]. These data were taken with a position sensitive detector and moderately course resolution (open-50'-40'R-120', where "R" indicates radial), where any splitting of the peaks would not be resolvable.

### B. Synchrotron powder diffraction

One of the intriguing magnetic properties of  $\text{YMn}_6\text{Sn}_6$  is the observation of two distinct incommensurate wave vectors for the zero-field magnetic structure, which has been observed in essentially all the magnetic neutron studies [14,16–18]. One obvious explanation would be that the samples grow in two slightly different structures or compositions, so there are two different samples under investigation. To ascertain if this might be the case, we carried out high-resolution synchrotron powder diffraction measurements to determine if more than one set of lattice parameters coexist, which could explain the presence of the two slightly different incommensurate magnetic modulations. However, the results definitively show that only one set of lattice parameters explains the data, and these are shown in Fig. 6(a). Excellent fits to the data were obtained,

and we find that the lattice parameters and volume [Fig. 6(b)] monotonically decrease with decreasing temperature, showing no discontinuity. Figure 6(c) shows an example of the calculated Rietveld refinement and data for 295 K. The refined parameters for all the data sets are displayed in Table I. There may be evidence for some slight inhomogeneity in the Sn content, since two data sets, at temperatures 90 K and 295 K, were taken at a slightly different conditions and different sampling positions than the rest. The total refined Sn content was found to be slightly lower for these two temperatures, with the main difference being the occupancy at the Sn3 site.

## C. Polarized neutron analysis at 290 K and 0 T

### 1. $\mathbf{Q} \parallel \mathbf{P}$

The spin-flip (SF) cross-section intensities,  $I^{+-}$  and  $I^{-+}$ , for magnetic Bragg peaks stemming from multiple zone centers are shown in Fig. 7, with the fits to the data shown as solid lines. The non-spin-flip (NSF) cross-section intensities,  $I^{++}$  and  $I^{--}$ , were also measured, but yielded no intensity, as expected for magnetic Bragg peaks in the  $\mathbf{Q} \cdot \mathbf{P} = 1$  configuration defined by a guide field of 1 mT. For each panel in Fig. 7, both wave vectors  $\mathbf{k}_1$  and  $\mathbf{k}_2$  are covered via a scan along the  $L$  direction, revealing that for a given wave vector the SF cross section that is most intense appears to depend on whether the peak is on the higher- or lower- $Q$  side of a given zone center. Scans along the  $HH$  direction in this  $(H, H, L)$  scattering plane were also performed to ensure the peaks were centered at the commensurate position in that direction. The integrated areas for each wave vector and cross section were evaluated and the ratios,  $I^{+-}/I^{-+}$ , are plotted for  $\mathbf{k}_1$  and  $\mathbf{k}_2$  in Figs. 8(a) and 8(b), respectively. As discussed further in the Discussion section, the only way for the two SF cross-section intensities to differ is in the presence of a spiral-type structure. Typically, in a centrosymmetric crystal, one would not see this difference due to multiple magnetic domains being evenly populated, and the difference here is due to the uneven population of the two possible chiral domains, referred to here as positive or negative chirality, where the chiral sign is defined by the sign of  $\mathbf{S}_i \times \mathbf{S}_j$  (where  $i$  and  $j$  here refer to nearest-neighbor noncollinear spins along the propagation direction). A least-squares calculation was performed to find the percentage of each chiral domain which best fits the  $I^{+-}/I^{-+}$  ratio data, and the results are shown as blue diamonds in Fig. 8. The dominant chirality for  $\mathbf{k}_1$  was found to be negative at 56.0%, and the dominant chirality for  $\mathbf{k}_2$  was found to be positive at 65.5%. Note that the chiralities for the two spirals are opposite, and comparable in magnitude, meaning that one spiral propagated (preferentially) in one direction, and the other in the opposite direction.

### 2. $\mathbf{Q} \perp \mathbf{P}$

In addition to the polarized neutron experiment configuration with the neutron polarization parallel to the scattering vector ( $\mathbf{Q} \parallel \mathbf{P}$ ), we also took data with the polarization perpendicular to the scattering vector and scattering plane ( $\mathbf{Q} \perp \mathbf{P}$ ). There is no chiral term in any of the scattering cross sections for this configuration, but magnetic scattering is allowed in the NSF channel when there is a component of the

TABLE I. Rietveld refined parameters from synchrotron powder diffraction data. The space group used for refinement was  $P6/mmm$  (191) and the atomic positions are Y (0, 0, 0), Mn ( $\frac{1}{2}$ , 0,  $z$ ), Sn1 ( $\frac{1}{3}$ ,  $\frac{2}{3}$ ,  $\frac{1}{2}$ ), Sn2 ( $\frac{1}{3}$ ,  $\frac{2}{3}$ , 0), and Sn3 (0, 0,  $z$ ). Temperatures denoted with \* were taken at a slightly different sampling position than the rest of the temperatures.

$T$ (K)	$R_{wp}$	$\chi^2$	$a$ (Å)	$c$ (Å)	Mn $z$ ( $z/c$ )	Sn3 $z$ ( $z/c$ )	Sn1 occ. (%)	Sn2 occ. (%)	Sn3 occ. (%)	$x$ ( $YMn_6Sn_x$ )
90*	9.40	1.70	5.518671(1)	8.994806(2)	0.24753(4)	0.33689(3)	97.12(8)	96.86(8)	97.83(9)	5.836(3)
200	10.0	2.24	5.529688(1)	9.008645(2)	0.24750(4)	0.33700(3)	98.16(9)	98.20(9)	99.68(9)	5.921(3)
240	9.93	2.12	5.534370(2)	9.014464(3)	0.24739(4)	0.33695(3)	98.30(8)	98.26(9)	99.64(9)	5.924(3)
295*	9.38	1.42	5.5410810(9)	9.022760(2)	0.24719(4)	0.33724(3)	97.74(8)	97.27(8)	98.32(8)	5.867(3)
320	9.98	1.94	5.544690(1)	9.027480(2)	0.24730(4)	0.33729(3)	98.05(8)	97.99(9)	99.94(9)	5.919(3)
340	9.60	1.78	5.547689(1)	9.031668(2)	0.24755(4)	0.33709(3)	97.88(8)	97.97(9)	100.08(9)	5.919(3)

spin parallel to the polarization vector; this gives directional information about the spin. Figure 9 shows the results of the data taken in this polarized geometry at 290 K for the magnetic Bragg peaks, (a)  $(0, 0, 2 + k_{z,n})$  and (b)  $(0, 0, 3 - k_{z,n})$ . There was no difference in intensity between the data from the two SF channels ( $+-$  and  $-+$ ) or between the two NSF channels ( $++$  and  $--$ ) for this polarization geometry, and thus the data from the two SF channels were averaged as well as the data from the two NSF channels. For both (a) and (b), there is also no difference between the integrated intensity of the SF and NSF data. This implies that the moments trace a circle as they spiral along the  $c$  axis, as opposed to an ellipse.

#### IV. DISCUSSION

Currently, there is not a satisfactory explanation for the coexistence of the two, almost equivalent, wave vectors found

in  $YMn_6Sn_6$  and in some doped variants [14,16–18]. One possibility suggested was that the magnetic structure has a nonconstant rotation of the moments, and the wave vectors observed were merely harmonics of a much smaller fundamental wave vector [17]. However, recent inelastic neutron-scattering measurements show that the observed wave vectors are, in fact, the magnetic zone center [22], making the modulated structure theory obsolete. An inhomogeneous distribution of two magnetic structures, which are almost energetically identical, could also be likely. Multiple ground states have been observed in intermetallics due to off-stoichiometry, such as the fluctuating Ni concentration in  $CeNi_{0.84}Sn_2$  which leads to two coexisting magnetic ground states [23], or the ground-state sensitivity to the Sn content in  $Ce_3Rh_4Sn_{13}$  [24]. Most similar is the itinerant antiferromagnet,  $Mn_3Sn$ , where two helical modulations coexist over a wide temperature range [25]. The incommensurate transition temperature and

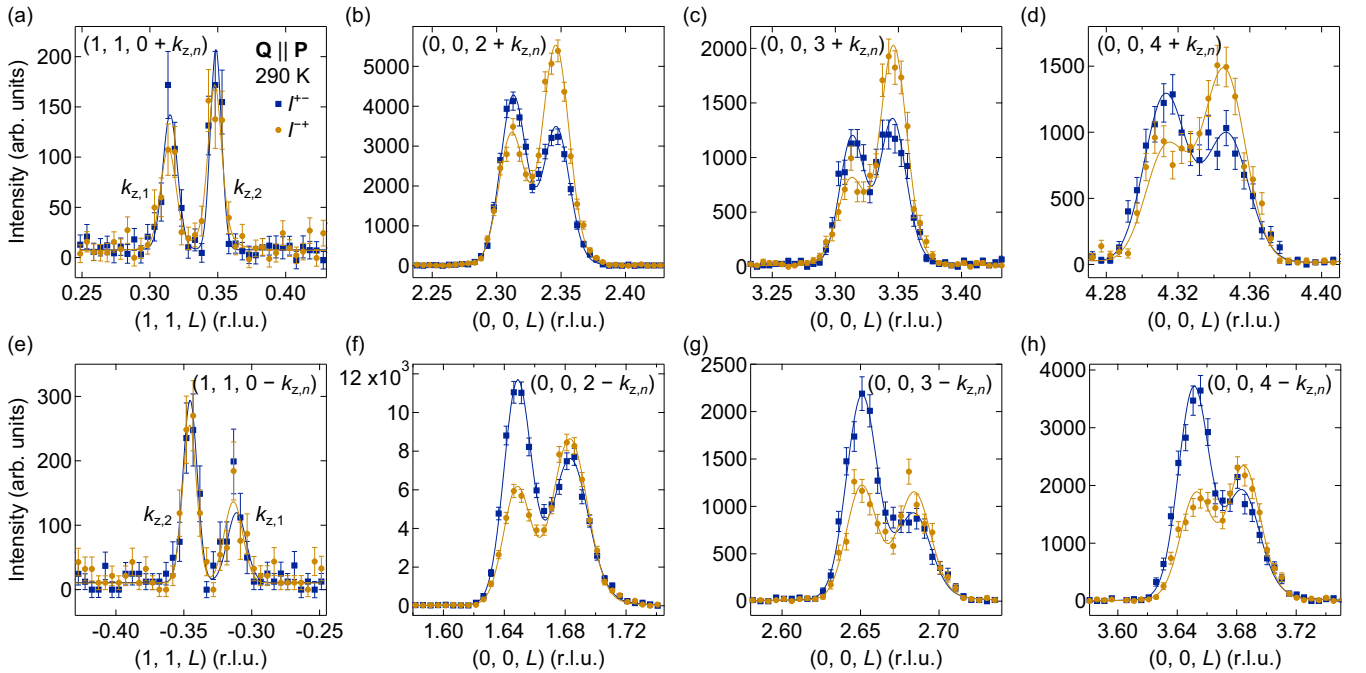


FIG. 7. Polarized neutron data with  $\mathbf{Q} \parallel \mathbf{P}$  at  $T = 290$  K showing scans which span the magnetic Bragg peaks associated with the two wave vectors,  $\mathbf{k}_i$  ( $i = 1, 2$ ,  $|\mathbf{k}_1| < |\mathbf{k}_2|$ ), discussed in the main text. Each panel displays the two spin-flip channels measured:  $+-$  (blue squares) and  $-+$  (orange circles). The top row, (a)–(d), shows Bragg peaks with zone-center  $+\mathbf{k}_i$  momenta, and the bottom row, (e)–(h), shows the corresponding zone-center  $-\mathbf{k}_i$  momenta.

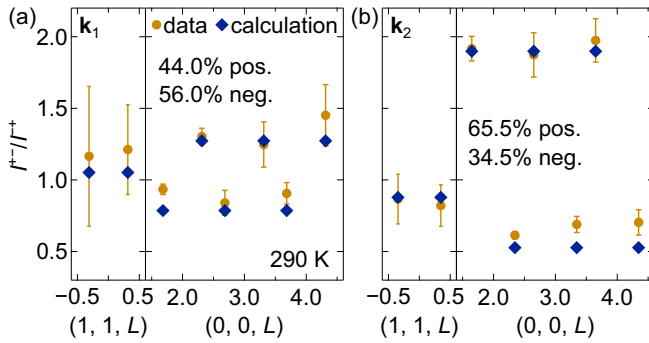


FIG. 8. Ratios of the  $\mathbf{Q} \parallel \mathbf{P}$  polarized neutron spin-flip channels,  $I^{+-}/I^{-+}$ , for the (a)  $\mathbf{k}_1$  wave vector and (b)  $\mathbf{k}_2$  wave vector. Ratios from the data, taken at  $T = 290$  K and shown as orange circles, represent the integrated intensities of fits to the data, as described in the main text. The calculated ratios, shown as blue diamonds, come from structure factor calculations for the given chiral domain populations.

wave-vector values were also shown to have a dependence on the annealing history, implying disorder may play a role in the magnetic structure [26]. However, our synchrotron powder diffraction data show that if chemical inhomogeneity were the root cause for the double wave vectors then there is no associated structural inhomogeneity in the form of a distribution of lattice parameters, and our neutron diffraction data show that the regions of homogeneous chemical compositions would have to be large enough to lead to long-range magnetic order (i.e.,  $>1000$  Å). This does not rule out macroscopic regions of varying Sn content as being responsible for the two propagation vectors and further chemical characterization on the Sn inhomogeneity across a crystal would shed more light on this possibility.

Also of note is the temperature dependence of the spirals' modulation lengths; the percent change in wave-vector component  $k_{z,n}$  between the onset of the incommensurate phase at 333 K and the base temperature measured (12 K in Ref. [14]) is quite large:  $-29\%$  for  $n = 1$  and  $-43\%$  for  $n = 2$ . Likely, this is due to the sensitivity of the spiral structures to the relative exchange pathway strengths  $J_1 - J_3$ , which in turn

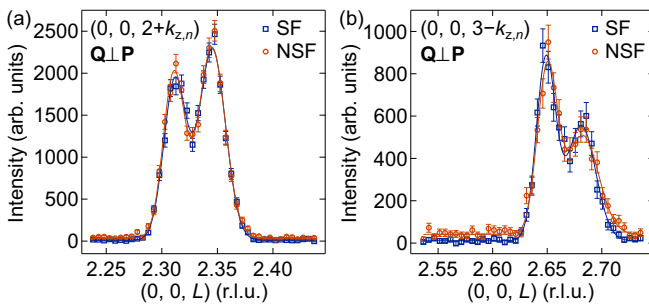


FIG. 9. Polarized neutron data with  $\mathbf{Q} \perp \mathbf{P}$  at 290 K for (a)  $(0, 0, 2 + k_{z,n})$  and (b)  $(0, 0, 3 - k_{z,n})$ . For both (a) and (b), there is no difference between the integrated intensity of the SF and NSF data. This implies that the moments trace a circle as they spiral along the  $c$  axis.

are temperature dependent due to the known importance of thermal fluctuations in this system.

The previous mapping of  $k_{z,1}$  and  $k_{z,2}$  with applied field in the  $ab$  plane [14] demonstrates that both magnetic structures are very close in energy to one another, with  $k_{z,1}$  consistently undergoing transitions at a slightly lower field than  $k_{z,2}$ . The room-temperature, low-field structure is an exception. The rapid disappearance of the  $k_{z,2}$  structure at 2 T as the commensurate structure appears suggests that  $k_{z,2}$  is transitioning to the commensurate structure, while the incommensurate  $k_{z,1}$  structure smoothly transitions to the FF state. The in-field commensurate structure is very similar to that at the Néel temperature, where the magnetic layers within a unit cell (across the  $\text{Sn}_3$  layer) are ferromagnetically coupled, and across the  $\text{Sn}_2\text{Y}$  layer are antiferromagnetically coupled. The in-field structure reported here is a canted variation of that structure, where all moments simply contribute to a net ferromagnetism pointed in the direction of the applied field.

Another deviation from the lower-temperature behavior is the absence of a spin-flop transition as field increases at 295 K. An antiferromagnet with magnetocrystalline anisotropy will have a spin-flop transition at a field proportional to  $\sqrt{\langle J \rangle K}$ , where in  $\text{YMn}_6\text{Sn}_6$ ,  $\langle J \rangle$  is the average out-of-plane Heisenberg exchange and  $K$  is the easy-plane magnetocrystalline anisotropy. It is expected that as temperature increases the spin-flop field would decrease, as observed via ac susceptibility measurements for temperatures lower than 295 K; instead, the distorted spiral (DS) to commensurate canted antiferromagnet shows no sign of a spin-flop transition, marked by the absence of any  $c$ -axis component in the reported structure. This is in contrast to the DS to TCS spin-flop phase transition seen at temperatures below 295 K and  $\approx 2$  T, where the in-plane field leads to a  $c$ -axis component of the moments. One explanation could lie in results from a small angle neutron-scattering study, which observed clear quasi-two-dimensional behavior in the form of spatial ferromagnetic fluctuations in the same temperature range as the absence of spin-flop behavior [27]. The report concludes that between  $\approx 260$  K and the paramagnetic state the system can best be described as a quasi-two-dimensional fluctuating ferromagnet, despite the spin structure having a net zero moment.

The low-temperature, high-field fanlike phase forms only below  $\approx 170$  K. Interestingly, this is also the lower-bound temperature for the observed THE, as thermal fluctuations are greatly reduced below this temperature, which is perhaps why the FL phase can find stability. This postulation comes from the theory that the THE mechanism is a result of chiral fluctuations stabilized by thermal fluctuations when an in-plane magnetic field is applied [14]. As discussed briefly in the Results section, the two fanlike models are almost indistinguishable, especially in the limit that  $\delta \rightarrow 0$  in model 1 (detailed magnetic structure factor calculations for both models are given in the Appendix). Model 1 can be justified as being more likely the correct structure, though. Figure 10 shows the energy for each model as the spins in layers 3, 4, 7, and 8 deviate from  $\delta = 0^\circ$ . Because the angles for spins 1, 2, 5, and 6 were found to be the same within error for both models, they were kept fixed at  $\pm 68^\circ$  for the calculations (as determined by the Rietveld refinement), which can be

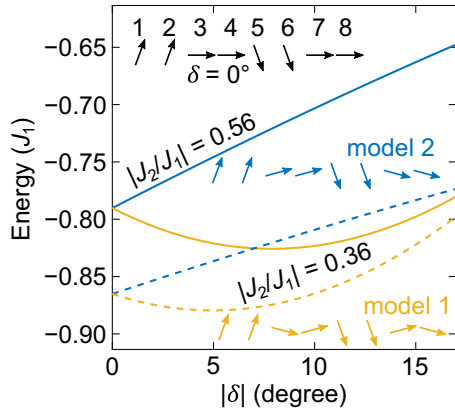


FIG. 10. Energy comparison between model 1 (orange) and model 2 (blue) as spins in layers 3, 4, 7, and 8 deviate from the  $\delta = 0^\circ$  axis, i.e., the applied field direction. The other spins are either  $\pm 68^\circ$  from the applied field direction, as determined by the Rivetveld refined structures. Two values for  $|J_2/J_1|$  are reported, where solid lines represent  $|J_2/J_1| = 0.56$  (full model), and dashed lines represent  $|J_2/J_1| = 0.36$  (reduced model). In both cases, the energy increases linearly as the spins deviate from the applied field direction for “model 2,” whereas the total energy initially decreases for “model 1.”

described by the equations

$$\text{Model 1 : } E = |J_2/J_1| \cos(68^\circ + \delta) - \cos(2\delta), \quad (1)$$

$$\text{Model 2 : } E = |J_2/J_1| \cos(68^\circ - \delta) - \cos(0^\circ), \quad (2)$$

where  $J_1$  is the ferromagnetic exchange between layers within the nuclear unit cell, and  $J_2$  is the antiferromagnetic exchange between layers on either side of the nuclear unit-cell boundary, and the energy is in units of  $J_1$ . Only nearest-neighbor interlayer exchange has been included in the calculation. The first term is the energy gain that results from spins connected by the  $J_2$  exchange not being antiparallel. The second term is the reduction in energy due to the relative alignment between spins 3 and 4 (or 7 and 8), and it can be seen that the maximum reduction in energy is realized when the spins are ferromagnetically coupled.

Although the zero-field magnetic structure in  $\text{YMn}_6\text{Sn}_6$  has been solved for quite some time [17], the polarized neutron diffraction performed here provides some much needed information in the study of this intriguing material. For example, helical and spin-density wave magnetic structures can often be difficult to distinguish from one another using unpolarized neutrons in a diffraction experiment (whether single crystal or powder diffraction). Even the addition of polarized neutrons with uniaxial polarization analysis may prove unhelpful depending on the scattering geometry with respect to the magnetic structure or if multiple helical domains are evenly populated. Here, polarized neutron diffraction results were able to show that the magnetic structure is helical and that the chiral domains are not evenly populated.

In a uniaxial polarized neutron experiment, there are four neutron scattering cross sections:  $I^{++}$ ,  $I^{+-}$ ,  $I^{-+}$ , and  $I^{--}$ . Nuclear coherent scattering never causes the reversal of the spin and hence is only observed in the  $I^{++}$  and  $I^{--}$  cross sec-

tions. When the scattering vector,  $\mathbf{Q}$ , is parallel to the neutron polarization,  $\mathbf{P}$ , all nuclear scattering is in the non-spin-flip channels,  $I^{++}$  or  $I^{--}$ , and all magnetic scattering is in the spin-flip channels,  $I^{+-}$  or  $I^{-+}$ , and hence can be distinguished unambiguously. Following the polarization analysis theory in Ref. [28], the scattering intensities  $I^{\pm\mp}$  are proportional to the spin-dependent cross sections:

$$\frac{d\sigma}{d\Omega_{\pm\mp}} = \sum_{i,j} e^{i\mathbf{k}\cdot(\mathbf{r}_i-\mathbf{r}_j)} p_i p_j^* [\mathbf{S}_{\perp i} \cdot \mathbf{S}_{\perp j} \mp i\hat{\mathbf{Z}} \cdot (\mathbf{S}_{\perp i} \times \mathbf{S}_{\perp j}^*)], \quad (3)$$

where the sum is over all magnetic atoms in the unit cell,  $p = (|r_0|/2)gf(Q)$  [ $r_0$  is the neutron magnetic moment multiplied by the classical electron radius,  $g$  is the Landé factor, and  $f(Q)$  is the magnetic form factor],  $\mathbf{S}_i$  are the magnetic moment vectors, and  $\hat{\mathbf{Z}}$  is a unit vector in the direction of the incoming neutron polarization. The last term in Eq. (3) is null for spin-density waves and other collinear structures. In fact, there is no way to obtain unequal  $I^{+-}$  and  $I^{-+}$  intensities on a magnetic Bragg peak without imaginary components in the basis vectors, which result in a spiral-type structure. Typically, for a centrosymmetric crystal, chiral domains will be present in equal populations because there is no energetic reason to favor one over the other. The scattering from the different domains then would result in equal  $I^{+-}$  and  $I^{-+}$  intensities. This is in contrast to single domain chiral crystals, where the sense (or sign) of the Dzyaloshinskii-Moriya interaction, if present, will pick out a single chiral domain, resulting in unequal  $I^{+-}$  and  $I^{-+}$  intensities.

The results of the polarized neutron study point towards the ability to manipulate or switch the chirality. Control of magnetic properties with an electric current or electric field has been well documented in multiferroics, materials exhibiting the magnetoelectric effect, and materials with broken inversion crystal symmetry. What can result in unequal spin-flip channel populations for centrosymmetric crystals is some external force to pick out a favorable chiral domain. For example, the simultaneous application of a magnetic field and electric current density was shown to control the chirality in  $\text{MnP}$  via spin transfer torque [29]. The chiral inequality for the  $\text{YMn}_6\text{Sn}_6$  sample used in this paper was surprising because no such external perturbation was intentionally applied. Strain or stress imparted onto the sample via mounting cannot be completely ruled out given that small uniaxial pressures can induce the anisotropy needed for preferential helical domains [30,31]. Since the established crystal structure is achiral, the observation of a preferential chiral domain requires additional breaking of the  $z \rightarrow -z$  mirror symmetry. For instance, this symmetry breaking may be affected through a particular defect ordering, or through asymmetric surface termination. In any event, this strong chirality not warranted by the underlying crystal structure is very interesting and deserves further investigation.

## V. SUMMARY

A magnetic field applied in the  $ab$  plane of  $\text{YMn}_6\text{Sn}_6$  leads to an extensive field-temperature phase diagram. This is owing to the delicate balance of competing interplane

exchange interactions between the magnetic kagome lattice layers. The neutron diffraction results presented here solve the magnetic structures for two of the previously identified phases. These are the commensurate CAF, appearing around room temperature and low fields, and the commensurate FL structure, which appears at low temperatures and high fields. Our paper also revealed that an additional incommensurate magnetic structure exists between the FL and FF phases, which explains the “phase I” region previously identified in ac susceptibility measurements. Two incommensurate wave vectors appear throughout many regions of the phase diagram, including at zero field, where both magnetic structures are the double-flat spiral, but with slightly differing periodicities. Via our high-resolution synchrotron powder diffraction measurements, we were able to show that the presence of the two wave vectors is likely an intrinsic feature of  $\text{YMn}_6\text{Sn}_6$ . Polarized neutron diffraction measurements showed that the zero-field incommensurate magnetic structures have preferential, but opposite, chiralities, which is a phenomenon usually reserved for lattices with broken inversion symmetry.

### ACKNOWLEDGMENTS

Synthesis and characterization work (N.J.G.) was supported by the U.S. Department of Energy, Office of Science, Basic Energy Sciences, Materials Science and Engineering Division. I.L.M. acknowledges support from the U.S. Department of Energy through Grant No. DE-SC0021089. Use of the Advanced Photon Source at Argonne National Laboratory was supported by the U.S. Department of Energy, Office of Science, Office of Basic Energy Sciences, under Contract No. DE-AC02-06CH11357. The identification of any commercial product or trade name does not imply endorsement or recommendation by the National Institute of Standards and Technology.

### APPENDIX: STRUCTURE FACTOR CALCULATIONS

To elucidate any differences between the low-temperature, high-field models (model 1 and model 2), we calculated the magnetic structure factor,  $\bar{F}_M$ , for various reflections in the  $(H, H, L)$  scattering plane. The geometry for calculating the models is shown in Fig. 11, where  $n$  ( $n = 1, 2, 3, \dots, 8$ ) refers to a layer of Mn moments in the magnetic unit cell ( $a, b, 4c$ ), and the  $n = 1$  layer is that which is closest to the  $c$ -axis origin (above that layer is  $n = 2$ , etc.). The vectors,  $\bar{S}_n$ , give the magnitude and direction of spins in layer  $n$ . All spins can be defined by  $\bar{S}_1$  and  $\bar{S}_3$ , which define the angles  $\gamma$  and  $\delta$ , respectively. Because neutrons are only sensitive to the component of spin which is perpendicular to the scattering vector,  $\bar{S}_\perp$ , we must also define the scattering vector in the same coordinate system as  $\bar{Q} = Q\hat{e}$ , where  $\hat{e} = e_x\hat{x} + e_y\hat{y} + e_z\hat{z}$  is a unit vector parallel to the scattering vector. In the  $(H, H, L)$  scattering geometry,  $e_y$  is always zero, and we have assumed moments are in the  $ab$  plane so that  $S_{z,n} = 0$ .  $\bar{S}_\perp$  can then be written as

$$\begin{aligned}\bar{S}_{\perp,n} &= \bar{S}_n - \hat{e}(\hat{e} \cdot \bar{S}_n) \\ &= S_{x,n}(1 - e_x^2)\hat{x} + S_{y,n}\hat{y} - e_x e_z S_{x,n}\hat{z}.\end{aligned}\quad (\text{A1})$$

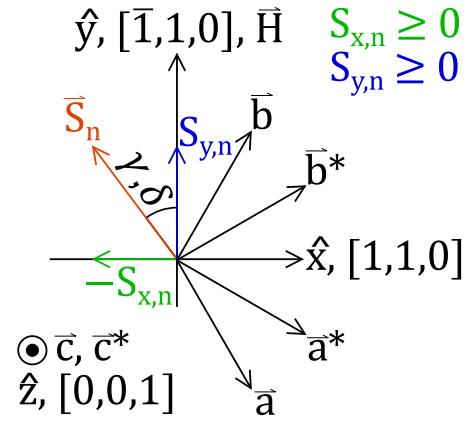


FIG. 11. The coordinate system used in calculating the magnetic structure factors, where  $\hat{x}$ ,  $\hat{y}$ , and  $\hat{z}$  are unit vectors which define a right-handed Cartesian coordinate system. The vector,  $\bar{S}_n$ , is the spin magnitude and direction for Mn moments in layer  $n$ , and  $\gamma$  and  $\delta$  are the values defined by the angle that  $\bar{S}_n$  makes with the applied field direction,  $\bar{H}$ .

In the following structure factor calculations,  $L$  is with respect to the magnetic unit cell (divide by 4 to get the equivalent reflection in the nuclear unit cell), and the prefactor is  $p = (|r_0|/2)gf(Q)$ , where  $r_0$  is the neutron magnetic moment multiplied by the classical electron radius,  $g$  is the Landé factor, and  $f(Q)$  is the magnetic form factor. The magnetic

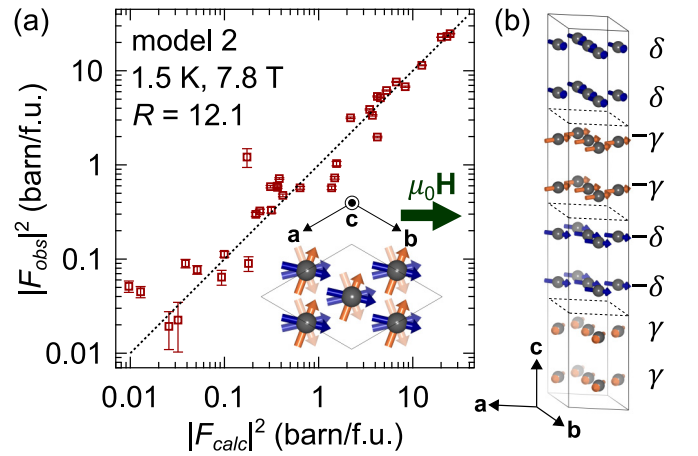


FIG. 12. Results for model 2 of the low-temperature, high-field fanlike phase with wave vectors,  $(0, 0, 0)$ ,  $(0, 0, 0.25)$ , and  $(0, 0, 0.5)$ . Data were taken at 1.5 K and 7.8 T in the  $(H, H, L)$  scattering plane. (a) The observed vs calculated magnetic structure factor squared in barn/formula unit (f.u.). The calculated result was obtained via Rietveld refinement for the magnetic intensity only. The inset shows the refined magnetic structure in the  $ab$  plane for 1.5 K and 7.8 T, where  $\gamma = 69(3)^\circ$  and  $\delta = 12(6)^\circ$ . Only Mn ions are shown (gray spheres), and the orange and blue arrows represent the two different angle magnitudes,  $\gamma$  and  $\delta$ , respectively, which define the moment directions away from the applied field direction. (b) The magnetic unit cell, where the dashed lines define the size of the nuclear unit cell.

structure factor for all  $(H, H, 0)$  peaks for both models is

$$|\bar{F}_M|_{H,H,0}^2 = 144|p|^2(S_{y,1} + S_{y,3})^2. \quad (\text{A2})$$

function] for both models is

$$|\bar{F}_M|_{H,H,L=2m}^2 = 144|p|^2\{\theta[(-1)^m] - (-1)^m \sin^2(4\pi mr_{c,1})\} [S_{y,1} + (-1)^m S_{y,3}]^2. \quad (\text{A3})$$

The magnetic structure factor for  $(H, H, L)$  peaks with  $L = 2m + 1$  for model 1 is

$$|\bar{F}_M|_{H,H,L=2m+1}^2 = 72|p|^2\left[(1 - e_x^2)^2 + e_x^2 e_z^2\right] \{S_{x,1}^2 + S_{x,3}^2 - 2S_{x,1}S_{x,3} \cos[4\pi(2m+1)r_{c,1}]\} \\ + (-1)^m (S_{x,1}^2 - S_{x,3}^2) \sin[4\pi(2m+1)r_{c,1}]. \quad (\text{A4})$$

The magnetic structure factor for  $(H, H, L)$  peaks with  $L = 2m + 1$  for model 2 is

$$|\bar{F}_M|_{H,H,L=2m+1}^2 = 72|p|^2\left[(1 - e_x^2)^2 + e_x^2 e_z^2\right] (S_{x,1}^2 + S_{x,3}^2) \{1 + (-1)^m \sin[4\pi(2m+1)r_{c,1}]\}. \quad (\text{A5})$$

The structure factors for both models have the same dependency on the  $S_y$  components, and only the  $S_y$  components, for  $(H, H, 0)$  and  $(H, H, L = 2m)$  peaks. These include the peaks coincident with the nuclear Bragg peaks and magnetic Bragg peaks at  $L = 0.5$  of the nuclear unit cell. The  $S_y$  components are those which are along the applied field direction. The models differ for the structure factors with  $L = 0.25$  or  $0.75$  of the nuclear unit cell. This can be seen by Eqs. (A4) and (A5). The structure factors for these peaks are only dependent

The magnetic structure factor for  $(H, H, L)$  peaks with  $L = 2m$  [where  $m = 1, 2, 3, \dots$ , and  $\theta(x)$  is the Heaviside step

on the  $S_x$  components of the spins, and it can be seen why the model 1 and model 2 refinements give practically the same goodness of fit: as  $S_{x,3} \rightarrow 0$ , which equivalently means  $\delta \rightarrow 0$ , Eqs. (A4) and (A5) converge. The refined  $\delta$  for model 1 is zero within error, and  $\delta$  for model 2 is  $12^\circ$  with a large standard deviation of  $\pm 6^\circ$ . Both the moment size and angle,  $\gamma$  (defined by  $\vec{S}_1$ ), are the same within error for model 1 and model 2. The model 2 refinement results are shown in Fig. 12.

- 
- [1] Y. Tokura and N. Nagaosa, Nonreciprocal responses from non-centrosymmetric quantum materials, *Nat. Commun.* **9**, 3740 (2018).
- [2] D. Grohol, K. Matan, J.-H. Cho, S.-H. Lee, J. W. Lynn, D. G. Nocera, and Y. S. Lee, Spin chirality on a two-dimensional frustrated lattice, *Nat. Mater.* **4**, 323 (2005).
- [3] A. Zorko, M. Pregelj, A. Potočnik, J. van Tol, A. Ozarowski, V. Simonet, P. Lejay, S. Petit, and R. Ballou, Role of Antisymmetric Exchange in Selecting Magnetic Chirality in  $\text{Ba}_3\text{NbFe}_3\text{Si}_2\text{O}_{14}$ , *Phys. Rev. Lett.* **107**, 257203 (2011).
- [4] A. K. Agyei and J. L. Birman, On the linear magnetoelectric effect, *J. Phys.: Condens. Mat.* **2**, 3007 (1990).
- [5] V. M. Edelstein, Magnetoelectric Effect in Polar Superconductors, *Phys. Rev. Lett.* **75**, 2004 (1995).
- [6] L. Ding, X. Xu, H. O. Jeschke, X. Bai, E. Feng, A. S. Alemany, J. Kim, F. Huang, Q. Zhang, X. Ding, N. Harrison, V. Zapf, D. Khomskii, I. I. Mazin, S.-W. Cheong, and H. Cao, Field-tunable toroidal moment in a chiral-lattice magnet, [arXiv:2103.01360](https://arxiv.org/abs/2103.01360) (2020).
- [7] G. Giteatpong, Y. Zhao, P. Piyawongwatthana, Y. Qiu, L. W. Harriger, N. P. Butch, T. J. Sato, and K. Matan, Nonreciprocal Magnons and Symmetry-Breaking in the Noncentrosymmetric Antiferromagnet, *Phys. Rev. Lett.* **119**, 047201 (2017).
- [8] T. Weber, J. Waizner, G. S. Tucker, L. Beddrich, M. Skoulatos, R. Georgii, A. Bauer, C. Pflleiderer, M. Garst, and P. Böni, Non-reciprocal magnons in non-centrosymmetric MnSi, *AIP Adv.* **8**, 101328 (2018).
- [9] T. Kurumaji, T. Nakajima, M. Hirschberger, A. Kikkawa, Y. Yamasaki, H. Sagayama, H. Nakao, Y. Taguchi, T.-h. Arima, and Y. Tokura, Skyrmion lattice with a giant topological Hall effect in a frustrated triangular-lattice magnet, *Science* **365**, 914 (2019).
- [10] T. Okubo, S. Chung, and H. Kawamura, Multiple- $q$  States and the Skyrmion Lattice of the Triangular-Lattice Heisenberg Antiferromagnet under Magnetic Fields, *Phys. Rev. Lett.* **108**, 017206 (2012).
- [11] A. O. Leonov and M. Mostovoy, Multiply periodic states and isolated skyrmions in an anisotropic frustrated magnet, *Nat. Commun.* **6**, 8275 (2015).
- [12] S. Ishiwata, T. Nakajima, J.-H. Kim, D. S. Inosov, N. Kanazawa, J. S. White, J. L. Gavilano, R. Georgii, K. M. Seemann, G. Brandl, P. Manuel, D. D. Khalyavin, S. Seki, Y. Tokunaga, M. Kinoshita, Y. W. Long, Y. Kaneko, Y. Taguchi, T. Arima, B. Keimer, and Y. Tokura, Emergent topological spin structures in the centrosymmetric cubic perovskite  $\text{SrFeO}_3$ , *Phys. Rev. B* **101**, 134406 (2020).
- [13] Q. Wang, K. J. Neubauer, C. Duan, Q. Yin, S. Fujitsu, H. Hosono, F. Ye, R. Zhang, S. Chi, K. Krycka, H. Lei, and P. Dai, Field-induced topological Hall effect and double-fan spin structure with a  $c$ -axis component in the metallic kagome anti-ferromagnetic compound  $\text{YMn}_6\text{Sn}_6$ , *Phys. Rev. B* **103**, 014416 (2021).
- [14] N. J. Ghimire, R. L. Dally, L. Poudel, D. C. Jones, D. Michel, N. T. Magar, M. Bleuel, M. A. McGuire, J. S. Jiang, J. F. Mitchell, J. W. Lynn, and I. I. Mazin, Competing magnetic phases and fluctuation-driven scalar spin chirality in the kagome metal  $\text{YMn}_6\text{Sn}_6$ , *Sci. Adv.* **6**, eabe2680 (2020).
- [15] E. Rosenfeld and N. Mushnikov, Double-flat-spiral magnetic structures: Theory and application to the  $\text{RMn}_6\text{X}_6$  compounds, *Physica B* **403**, 1898 (2008).

- [16] G. Venturini, B. E. Idrissi, and B. Malaman, Magnetic properties of  $\text{RMn}_6\text{Sn}_6$  ( $R = \text{Sc}, \text{Y}, \text{Gd-Tm}, \text{Lu}$ ) compounds with  $\text{HfFe}_6\text{Ge}_6$  type structure, *J. Magn. Magn. Mater.* **94**, 35 (1991).
- [17] G. Venturini, D. Fruchart, and B. Malaman, Incommensurate magnetic structures of  $\text{RMn}_6\text{Sn}_6$  ( $R = \text{Sc}, \text{Y}, \text{Lu}$ ) compounds from neutron diffraction study, *J. Alloy Compd.* **236**, 102 (1996).
- [18] L. Eichenberger, G. Venturini, B. Malaman, L. Nataf, F. Baudalet, and T. Mazet, Commensurate-incommensurate magnetic phase transition in the new  $\text{Yb}_{1-x}\text{Lu}_x\text{Mn}_6\text{Sn}_6$  compounds, *J. Alloy Compd.* **695**, 286 (2017).
- [19] J. W. Lynn, Y. Chen, S. Chang, Y. Zhao, S. Chi, W. Ratcliff II, B. G. Ueland, and R. W. Erwin, Double-focusing thermal triple-axis spectrometer at the NCNR, *J. Res. Natl. Inst. Stan.* **117**, 61 (2012).
- [20] J. Rodríguez-Carvajal, Recent advances in magnetic structure determination by neutron powder diffraction, *Physica B* **192**, 55 (1993).
- [21] W. Chen, G. Armstrong, Y. Chen, B. Collett, R. Erwin, T. Gentile, G. Jones, J. Lynn, S. McKenney, and J. Steinberg,  $^3\text{He}$  spin filters for a thermal neutron triple axis spectrometer, *Physica B* **397**, 168 (2007).
- [22] H. Zhang, X. Feng, T. Heitmann, A. I. Kolesnikov, M. B. Stone, Y.-M. Lu, and X. Ke, Topological magnon bands in a room-temperature kagome magnet, *Phys. Rev. B* **101**, 100405(R) (2020).
- [23] P. Schobinger-Papamantellos, J. Rodríguez-Carvajal, K. Prokes, and K. H. J. Buschow, Magnetic properties of studied by magnetization and neutron diffraction, *J. Phys.-Condens. Mat.* **8**, 8635 (1996).
- [24] A. Slebarski, B. D. White, M. Fijalkowski, J. Goraus, J. J. Hamlin, and M. B. Maple, Electronic, magnetic, and electric transport properties of  $\text{Ce}_3\text{Rh}_4\text{Sn}_{13}$  and  $\text{Ce}_3\text{Co}_4\text{Sn}_{13}$ : A comparative study, *Phys. Rev. B* **86**, 205113 (2012).
- [25] J. W. Cable, N. Wakabayashi, and P. Radhakrishna, A neutron study of the magnetic structure of  $\text{Mn}_3\text{Sn}$ , *Solid State Commun.* **88**, 161 (1993).
- [26] G. G. Marcus, Incommensurate metallic magnetism in  $\text{CeAuSb}_2$  and  $\text{Mn}_3\text{Sn}$ , Ph.D. thesis, Johns Hopkins University, 2018.
- [27] A. A. Bykov, Y. O. Chetverikov, A. N. Pirogov, and S. V. Grigor'ev, Quasi-two-dimensional character of the magnetic order-disorder transition in  $\text{YMn}_6\text{Sn}_6$ , *JETP Lett.* **101**, 699 (2015).
- [28] W. Williams, *Polarized Neutrons*, Oxford Science Publications (Clarendon, Oxford, 1988).
- [29] N. Jiang, Y. Nii, H. Arisawa, E. Saitoh, and Y. Onose, Electric current control of spin helicity in an itinerant helimagnet, *Nat. Commun.* **11**, 1601 (2020).
- [30] M. Deutsch, P. Bonville, A. V. Tsvyashchenko, L. N. Fomicheva, F. Porcher, F. Damay, S. Petit, and I. Mirebeau, Stress-induced magnetic textures and fluctuating chiral phase in  $\text{MnGe}$  chiral magnet, *Phys. Rev. B* **90**, 144401 (2014).
- [31] A. Chacon, A. Bauer, T. Adams, F. Rucker, G. Brandl, R. Georgii, M. Garst, and C. Pfleiderer, Uniaxial Pressure Dependence of Magnetic Order in  $\text{MnSi}$ , *Phys. Rev. Lett.* **115**, 267202 (2015).